The Astrophysical Journal, 611:1021–1032, 2004 August 20

HYDRODYNAMIC EFFECTS IN INTERNAL SHOCK OF RELATIVISTIC OUTFLOWS

Motoki Kino,[1] Akira Mizuta,[2] and Shoichi Yamada[3]
Received 2003 December 3; accepted 2004 April 27

ABSTRACT

We study both analytically and numerically hydrodynamic effects of two colliding shells, the simplified models of internal shock in various relativistic outflows such as gamma-ray bursts and blazars. We pay particular attention to three interesting cases: a pair of shells with the same rest-mass density (''equal rest-mass density''), a pair of shells with the same rest mass (''equal mass''), and a pair of shells with the same bulk kinetic energy (''equal energy'') measured in the interstellar medium frame. We find that the density profiles are significantly affected by the propagation of rarefaction waves. A split feature appears at the contact discontinuity of two shells for the equal-mass case, while no significant split appears for the equal-energy and equal rest-mass density cases. The shell spreading within a few 10% of the speed of light is also shown as a notable aspect caused by rarefaction waves. The conversion efficiency of bulk kinetic energy to internal energy is numerically evaluated. The time evolutions of the efficiency show deviations from the widely used inelastic two-point mass-collision model.

Subject headings: galaxies: jets — gamma rays: bursts — gamma rays: theory — radiation mechanisms: nonthermal — shock waves

1. INTRODUCTION

The internal shock scenario proposed by Rees (1978) is one of the most promising models for explaining the observational feature of relativistic outflows, as in gamma-ray bursts (GRBs) and blazars (e.g., Rees & Meszaros 1994; Spada et al. 2001). In this scenario, the bulk kinetic energy of the outflowing plasma is converted into thermal energy and nonthermal particle energy by shock dissipation and particle acceleration, respectively, and explains the great power of these objects. Based on this scenario, many authors have attempted to link the observed temporal profiles to multiple internal interactions (e.g., Kobayashi et al. 1997, hereafter KPS97; Panaitescu et al. 1997; Tanihata et al. 2003; Nakar & Piran 2002, hereafter NP02), looking for crucial hints on the central engine of these relativistic outflows.

Most of the previous works focus on the comparison with the observed light curves and model predictions employing a simple inelastic collision of two-point masses (KPS97), and little attention has been paid to hydrodynamic processes in shell collision. However, it is obvious that, in the case of relativistic shocks, the timescales in which shock and rarefaction waves cross the shells are comparable to the dynamical timescale Δ'/c, where Δ' is the shell width measured in the comoving frame of the shell and c is the speed of light. Since the timescales of observations of these relativistic outflows (e.g., Takahashi et al. 2000 for blazar jets; Fishman & Meegan 1995 for GRBs) are much longer than the dynamical timescales, the light curves should contain the footprints of these hydrodynamic wave propagations. Thus, it is very interesting to clarify the difference between the simple two-point mass-collision (hereafter two-mass collision) model and the hydrodynamic treatment. The recent study by Kobayashi & Sari (2001, hereafter KS01) reports that collided shells are reflected from each other by thermal expansion. Since they perform a hydrodynamic simulation and show the reflection feature for a single case, the details of propagations of rarefaction waves for various cases of collisions is not discussed. The aim of this paper is to clarify the hydrodynamic effects including the propagations of rarefaction wave. As the simplest case, we explore the hydrodynamics of two-shell collisions in the internal shock model. Since we are mainly interested in the hydrodynamic processes themselves, it is beyond the scope of this paper to make a detailed comparison of the observed phenomena with the model results.

We consider the time evolution of two colliding shells in relativistic hydrodynamics in § 2. In § 3 we discuss the application to GRBs and blazars. The summary and discussion are given in § 4.

2. HYDRODYNAMICS

Here we consider the hydrodynamics of the two-shell interactions. Our intention is to derive analytically various timescales for shocks and rarefaction waves crossing the shells. The fundamentals of relativistic shocks are given by Landau & Lifshitz (1959) and Blandford & McKee (1976). Our main assumptions are as follows: (1) we adopt a planar one-dimensional shock analysis and neglect radiative coolings for simplicity, (2) we neglect the effect of magnetic fields, and (3) we limit our attention to shells with relativistic speeds. We are currently planing two-dimensional studies. The role of magnetic fields is still under debate. A multifrequency analysis of TeV blazars shows that the energy density of the magnetic field is smaller than that of nonthermal electrons (Kino et al. 2002). As for assumption 3, it is self-evident that the relativistic regime is most important, since emissions from GRBs and blazars show a substantial Doppler boost.

2.1. *Shock Jump Condition*

In Figure 1 we draw a schematic mass density profile during the shock propagation in the interactions of rapid and

[1] International School for Advanced Studies (SISSA), via Beirut 2-4, 34014 Trieste, Italy.
[2] Institute of Laser Engineering, Osaka University, Suita, Osaka 565-0871, Japan.
[3] Science and Engineering, Waseda University, Shinjyuku, Tokyo 169-8555, Japan.

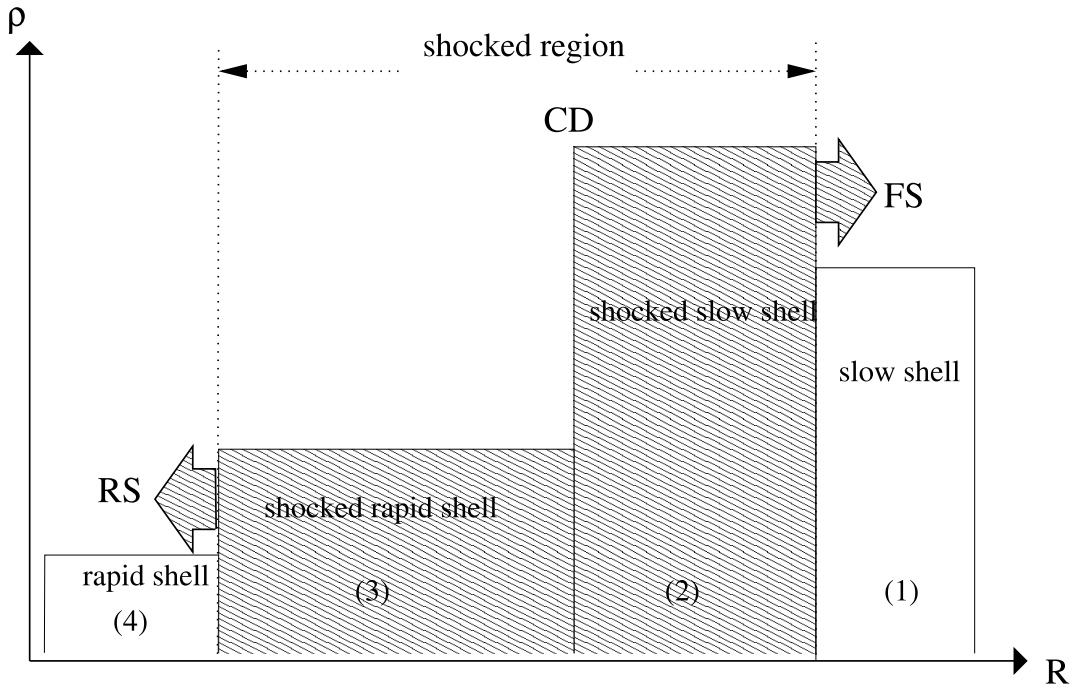

FIG. 1.—Sketch of a two-shell collision in which a rapid shell catches up with a slower one at the CD frame. Forward and reverse shocks (FS and RS) propagate from the contact discontinuity (CD). We employ the conventional numbering for each region in the study of GRBs (e.g., Piran 1999).

slow shells. Two shocks are formed: a reverse shock that goes into the rapid shell and a forward shock that propagates into the slow shell. There are four regions: (1) the unshocked slow shell, (2) the shocked slow shell, (3) the shocked rapid shell, and (4) the unshocked rapid shell. Thermodynamic quantities, such as rest-mass density ρ, pressure P, and internal energy density e, are measured in the fluid rest frames. We use the terminology of *regions* i ($i = 1$, 2, 3, and 4) and *position of discontinuity* j ($j =$ FS, CD, and RS) where FS, CD, and RS stand for the forward shock front, contact discontinuity, and reverse shock front, respectively. The fluid velocity and Lorentz factor in region i measured in the interstellar medium (ISM) rest frame are expressed as $v_i (= \beta_i c)$ and Γ_i, respectively. The relative velocity and Lorentz factor of the fluids in regions i and j are denoted as $v_{ij} (= -v_{ji} = \beta_{ij} c = -\beta_{ji} c)$ and $\Gamma_{ij} (= \Gamma_{ji})$, respectively. Throughout this work, we use the assumption of $\Gamma_i \gg 1$.

We first count the numbers of quantities and the shock jump conditions. Each region is specified by three physical quantities: rest-mass density ρ_i, pressure P_i, and velocity v_i measured in the ISM rest frame. Forward and reverse shock speeds measured in the frame of unshocked regions (i.e., regions 1 and 4, respectively) are two other quantities. In all, there are $3 \times 4 + 2 = 14$ physical quantities. The total number of the jump conditions at FS, RS, and CD is $3 + 3 + 2 = 8$. Hence, given $3 + 3 = 6$ upstream quantities for each shock, we can obtain the eight remaining downstream quantities by using eight jump conditions.

Following Blandford & McKee (1976), we consider the limit of strong shock, $P_2/n_2 \gg P_1/n_1$, and adopt the assumption that the upstream matter is cold. As an equation of state (EOS), we take

$$P_i = (\hat{\gamma}_i - 1)(e_i - \rho_i), \tag{1}$$

where $\hat{\gamma}_i$ is an adiabatic index. The jump conditions for the forward shock are written as follows:

$$\Gamma_{\rm FS1}^2 = \frac{(\Gamma_{12} + 1)[\hat{\gamma}_2(\Gamma_{12} - 1) + 1]^2}{\hat{\gamma}_2(2 - \hat{\gamma}_2)(\Gamma_{12} - 1) + 2},$$
$$e_2 = \Gamma_{12}\rho_2, \quad \frac{\rho_2}{\rho_1} = \frac{\hat{\gamma}_2\Gamma_{12} + 1}{\hat{\gamma}_2 - 1}, \tag{2}$$

where $\Gamma_{12} = \Gamma_1\Gamma_2(1 - \beta_1\beta_2)$ and $\Gamma_{\rm FS1}$ is the Lorentz factor of forward shock measured in the rest frame of the unshocked slow shell. In the relativistic limit, the adiabatic index is $\hat{\gamma}_2 = 4/3$. Using the same assumptions as in the forward shock, the jump conditions for the reverse shock are given by

$$\Gamma_{\rm RS4}^2 = \frac{(\Gamma_{34} + 1)[\hat{\gamma}_3(\Gamma_{34} - 1) + 1]^2}{\hat{\gamma}_3(2 - \hat{\gamma}_3)(\Gamma_{34} - 1) + 2},$$
$$e_3 = \Gamma_{34}\rho_3, \quad \frac{\rho_3}{\rho_4} = \frac{\hat{\gamma}_3\Gamma_{34} + 1}{\hat{\gamma}_3 - 1}, \tag{3}$$

where $\Gamma_{34} = \Gamma_3\Gamma_4(1 - \beta_3\beta_4)$ and $\Gamma_{\rm RS4}$ is the Lorentz factor of the reverse shock measured in the rest frame of the unshocked rapid shell. The equality of pressures and velocities across the contact discontinuity gives

$$P_2 = P_3, \quad \Gamma_2 = \Gamma_3. \tag{4}$$

Before a shock breakout, $\Gamma_2 = \Gamma_3 = \Gamma_{\rm CD}$ is satisfied. It may be useful to introduce the ratio $f \equiv \rho_4/\rho_1$, which can be obtained from $P_2 = P_3$, as

$$f \equiv \frac{\rho_4}{\rho_1} = \frac{(\hat{\gamma}_2\Gamma_{12} + 1)(\Gamma_{12} - 1)}{(\hat{\gamma}_3\Gamma_{34} + 1)(\Gamma_{34} - 1)}. \tag{5}$$

Throughout this paper, we set $P_1 = P_4 = 0$. Then we take ρ_1, ρ_4, Γ_1, and Γ_4 as the four remaining upstream parameters.

Then, with the eight shock conditions given above, we can obtain eight downstream quantities: ρ_2, e_2, v_2, $v_{\rm FS}$, ρ_3, e_3, v_3, and $v_{\rm RS}$.

2.2. *Timescales of Wave Propagations*

Here we evaluate seven timescales of relevance when the shock and rarefaction waves cross the colliding shells. They are useful for understanding the hydrodynamic evolution of two-shell collisions. We measure these timescales in the rest frame of CD (hereafter CD frame) because it facilitates comparison with each other. In contrast, most of the previous papers used the ISM frame to measure the crossing time of the shock (e.g., Sari & Piran 1995; Panaitescu et al. 1997). Here we need to introduce new physical parameters, the shell widths measured in the ISM frame, Δ_r and Δ_s, where subscripts r and s represent rapid and slow shells, respectively. In the ISM frame, the upstream parameters are as follows: Lorentz factors $\Gamma_r(=\Gamma_4)$ and $\Gamma_s(=\Gamma_1)$, and rest-mass densities ρ_r and ρ_s. With $2+4=6$ physical parameters, we can uniquely specify the initial condition. Note that regions 1 and 4 disappear after FS and RS break out, respectively.

In the CD frame, we rewrite them as Δ'_r, Δ'_s, Γ'_r $(=\Gamma'_4=\Gamma_{34})$, and $\Gamma'_s(=\Gamma'_1=\Gamma_{12})$ during the shock propagation in the shells. After the shock breaks out of the shell, the velocity is not uniform and determined by the propagation of rarefaction wave. Note that once we choose the CD frame, Γ'_4 and Γ'_1 are not independent of each other (see, e.g., eq. [8]).

The time in which FS crosses the slow shell, $t'_{\rm FS}$, is given by

$$t'_{\rm FS}=\frac{\Delta'_s}{|\beta'_1|+|\beta'_{\rm FS}|}=\Delta'_s\left\{|\beta'_1|+\left[1-\frac{1}{\Gamma'^2_1\Gamma^2_{\rm FS1}(1-|\beta'_1||\beta_{\rm FS1}|)^2}\right]^{1/2}\right\}^{-1}, \quad (6)$$

where we use equation (2) and $\beta'^2_{\rm FS}=1-1/\Gamma'^2_{\rm FS}$. Thus, we can express $t'_{\rm FS}$ as a function of model parameters and Γ'_1, which is also given implicitly from the model parameters. Similarly, the RS crossing time in the rapid shell, $t'_{\rm RS}$, is

$$t'_{\rm RS}=\frac{\Delta'_r}{|\beta'_4|+|\beta'_{\rm RS}|}=\Delta'_r\left\{|\beta'_4|+\left[1-\frac{1}{\Gamma'^2_4\Gamma^2_{\rm RS4}(1-|\beta'_4||\beta_{\rm RS4}|)^2}\right]^{1/2}\right\}^{-1}, \quad (7)$$

where we use equation (3) and $\beta'^2_{\rm RS}=1-1/\Gamma'^2_{\rm RS}$. It is important to note that Γ'_1 and Γ'_4 are not independent but related by

$$\Gamma'_4=\frac{-f(1-\hat\gamma_3)+\sqrt{f^2(1-\hat\gamma_3)^2+4f\hat\gamma_3\left[(\Gamma'_1-1)(\hat\gamma_2\Gamma'_1+1)+f\right]}}{2f\hat\gamma_3}. \quad (8)$$

It is expected that after FS has crossed the slow shell, a rarefaction wave (hereafter FR) propagates into the shocked slow shell (e.g., Panaitescu et al. 1997). The sound speed is given by (e.g., Mihalas & Mihalas 1984)

$$c_s^2=\left(\frac{\partial P}{\partial e}\right)_{\rm ad}=\frac{\hat\gamma P}{e+P}. \quad (9)$$

Thus, the time at which FR reaches CD, $t'_{\rm FR\text{-}CD}$, is given by

$$t'_{\rm FR\text{-}CD}=t'_{\rm FS}+\frac{\Delta'_{s,\rm FS}}{c_{s2}}=t'_{\rm FS}+\Delta'_s\Gamma'_1\frac{\hat\gamma_2-1}{\hat\gamma_2\Gamma'_1+1}\left[\frac{\hat\gamma_2(\hat\gamma_2-1)(\Gamma'_1-1)}{\hat\gamma_2\Gamma'_1-\hat\gamma_2+1}c^2\right]^{-1/2}, \quad (10)$$

where $\Delta'_{s,\rm FS}$ is the width of the slow shell just after FS reaches the end of the shell. This is obtained by the mass conservation (e.g., Spada et al. 2001), where $(\hat\gamma_2-1)/(\hat\gamma_2\Gamma'_1+1)$ is the compression factor of the slow shell and Γ'_1 is the factor from the Lorentz contraction. Similarly, the corresponding time, $t'_{\rm RR\text{-}CD}$, at which the rarefaction wave (hereafter RR) generated at the RS breakout reaches CD is given by

$$t'_{\rm RR\text{-}CD}=t'_{\rm RS}+\frac{\Delta'_{r,\rm RS}}{c_{s3}}=t'_{\rm RS}+\Delta'_r\Gamma'_4\frac{\hat\gamma_3-1}{\hat\gamma_3\Gamma'_4+1}\left[\frac{\hat\gamma_3(\hat\gamma_3-1)(\Gamma'_4-1)}{\hat\gamma_3\Gamma'_4-\hat\gamma_3+1}c^2\right]^{-1/2}. \quad (11)$$

In the case of $t'_{\rm RR\text{-}CD}>t'_{\rm FR\text{-}CD}$, only $t'_{\rm FR\text{-}CD}$ is an actual time, and $t'_{\rm RR\text{-}CD}$ is a virtual time that does not exist in reality. The opposite case is also true.

In the case of $t'_{\rm RR\text{-}CD}<t'_{\rm FR\text{-}CD}$, we have the time at which two rarefaction waves collide, $t'_{\rm RR\text{-}FR}$, as

$$t'_{\rm RR\text{-}FR}\sim t'_{\rm RR\text{-}CD}+\frac{\Delta'_{s,\rm RR\text{-}CD}}{2c_{s2}}\sim t'_{\rm RR\text{-}CD}+\frac{\Delta'_s\Gamma'_1}{2c_{s2}}\frac{\hat\gamma_2-1}{\hat\gamma_2\Gamma'_1+1}\left(\frac{t'_{\rm FR\text{-}CD}-t'_{\rm RR\text{-}CD}}{t'_{\rm FR\text{-}CD}-t'_{\rm FS}}\right), \quad (12)$$

where $\Delta'_{s,\rm RR\text{-}CD}$ is the width of the part of slow shell through which FR has not passed yet at $t'_{\rm RR\text{-}CD}$. Since both RR and FR propagate at the speed c_{s2} after $t'_{\rm RR\text{-}CD}$, the above equation includes a factor of 2. Note that after the rarefaction wave crosses CD, the pressure gradient appears at CD. As a result, CD begins to move from $x'=0$ in the CD frame. Thus, equations (12), (13), (14), and (15) are approximate estimations. Similarly, in the case of $t'_{\rm FR\text{-}CD}<t'_{\rm RR\text{-}CD}$, we have

$$t'_{\rm RR\text{-}FR}\sim t'_{\rm FR\text{-}CD}+\frac{\Delta'_{r,\rm FR\text{-}CD}}{2c_{s3}}\sim t'_{\rm FR\text{-}CD}+\frac{\Delta'_r\Gamma'_4}{2c_{s3}}\frac{\hat\gamma_3-1}{\hat\gamma_3\Gamma'_4+1}\left(\frac{t'_{\rm RR\text{-}CD}-t'_{\rm FR\text{-}CD}}{t'_{\rm RR\text{-}CD}-t'_{\rm RS}}\right). \quad (13)$$

The timescale in which RR catches up with the propagating forward shock (FS), $t'_{\rm RR\text{-}FS}$, can be estimated as

$$t'_{\rm RR\text{-}FS}\sim\frac{c_{s,2}t'_{\rm RR\text{-}CD}}{c_{s2}-\beta'_{\rm FS}c}. \quad (14)$$

Similarly, the timescale in which FR catches up with the reverse shock (RS) is approximated as

$$t'_{\rm FR\text{-}RS}\sim\frac{c_{r,3}t'_{\rm FR\text{-}CD}}{c_{s3}-\beta'_{\rm RS}c}. \quad (15)$$

2.3. *Numerical Simulation*

We complementarily perform the special relativistic hydrodynamic simulations. The detail of the code is given in Mizuta et al. (2004). To sum up, the code is based on an approximate relativistic Riemann solver. The numerical flux is derived from Marquina's flux formula (Donat & Marquina 1996). This code is originally second order in space using the so-called MUSCL method. In this study, however, this is slightly compromised for numerical stability. We assume plane symmetry and treat one-dimensional motions of shells. In discussing the propagation of shock and rarefaction waves, we choose the CD frame. Given the ratio Γ_r/Γ_s in the ISM frame and the value of Γ_s, we can determine the Lorentz transformation to the CD frame easily because the CD Lorentz factor $\Gamma_{\rm CD}(=\Gamma_2=\Gamma_3)$ measured in the ISM frame can be derived by solving equation (5). We should note that the number of free parameters is reduced from six to five because we have already fixed the frame. As for the EOS, we assume for simplicity that $\hat{\gamma}_3=\hat{\gamma}_2=4/3$ for $\Gamma_{34}>2$ and $\hat{\gamma}_3=\hat{\gamma}_2=5/3$ otherwise. Although this simplification gives slightly inaccurate estimation of the speeds of wave propagations, there is little effect on our conclusions in this work.

We start the calculation at $t=0$ when the collision of two shells has just begun. Throughout this paper, we set $\Delta_s'/c=1$ and $\rho_r=1$ as units in numerical simulations. Initially, two shells have opposite velocities, namely, $v_r'>0$ and $v_s'<0$. In § 2.2 we did not impose any conditions for the plasma surrounding the two shells. We only assumed that the boundary of each shell will be kept intact during the passage of shocks and rarefaction waves. For our numerical runs, we put plasma of low rest-mass density ($10^{-4}\ll 1,\ \rho_s/\rho_r$) outside of the two shells. They have the same velocity and pressure as the adjacent shell. At first, the boundary condition at the left boundary is a steady inflow of dilute plasma. When the reverse shock or the rarefaction wave reaches the rapid shell's boundary, the velocity of the dilute plasma is set to be zero instantaneously to reduce the effect of the interaction between the shock and the dilute plasma. At the same time, the left boundary condition is set to be a free outflow. The treatment of the right-side dilute plasma and the boundary condition is the same as that of the left side.

3. SHELL DYNAMICS AFTER COLLISION

3.1. *Shell Splitting*

3.1.1. *General Consideration*

Here we classify the types of mass density profiles in the merged shell based on the order of the times obtained in § 2.2. Table 1 gives the complete set of possible orders. Although there are various cases in the orders, the density profile in particular, the splitting feature is governed by two criteria.

1. When $t'_{\rm RR\text{-}CD}<t'_{\rm FR\text{-}CD}$ for $\rho_r>\rho_s$ or $t'_{\rm FR\text{-}CD}<t'_{\rm RR\text{-}CD}$ for $\rho_s>\rho_r$ is satisfied, the splitting occurs at CD, since the rarefaction wave going from the larger density region (region 2) into the smaller density region (region 3) makes a dip in the latter region.
2. When a pair of rarefaction waves propagating in opposite directions collide, the density begins to decrease at the collision point and the splitting feature emerges. Hence, the existence of $t_{\rm RR\text{-}FR}$ implies a splitting feature.

Based on these two criteria, the mass density profile is classified into four types and shown in Figure 2. If both criteria are satisfied, then the mass density has triple peaks. We show the corresponding schematic picture of spacetime diagram in Figure 3. If only one criterion is met, then the double-peaked profile is realized. When neither condition is satisfied, the single peak is obtained.

TABLE 1
VARIOUS TYPES OF EVOLUTION

Number	Timescale[a]	Profile[b]
	$\rho_s>\rho_r$	
1	$t'_{\rm RS}<t'_{\rm RR\text{-}CD}<t'_{\rm RR\text{-}FS}$	S
2	$t'_{\rm RS}<t'_{\rm RR\text{-}CD}<t'_{\rm FS}<t'_{\rm RR\text{-}FR}$	D1
3	$t'_{\rm RS}<t'_{\rm FS}<t'_{\rm RR\text{-}CD}<t'_{\rm RR\text{-}FR}$	D1
4	$t'_{\rm RS}<t'_{\rm FS}<t'_{\rm FR\text{-}CD}<t'_{\rm RR\text{-}FR}$	T
5	$t'_{\rm FS}<t'_{\rm FR\text{-}CD}<t'_{\rm FR\text{-}RS}$	D2
6	$t'_{\rm FS}<t'_{\rm FR\text{-}CD}<t'_{\rm RS}<t'_{\rm RR\text{-}FR}$	T
7	$t'_{\rm FS}<t'_{\rm RS}<t'_{\rm FR\text{-}CD}<t'_{\rm RR\text{-}FR}$	T
8	$t'_{\rm FS}<t'_{\rm RS}<t'_{\rm RR\text{-}CD}<t'_{\rm RR\text{-}FR}$	D1
	$\rho_s<\rho_r$	
9	$t'_{\rm RS}<t'_{\rm RR\text{-}CD}<t'_{\rm RR\text{-}FS}$	D2
10	$t'_{\rm RS}<t'_{\rm RR\text{-}CD}<t'_{\rm FS}<t'_{\rm RR\text{-}FR}$	T
11	$t'_{\rm RS}<t'_{\rm FS}<t'_{\rm RR\text{-}CD}<t'_{\rm RR\text{-}FR}$	T
12	$t'_{\rm RS}<t'_{\rm FS}<t'_{\rm FR\text{-}CD}<t'_{\rm RR\text{-}FR}$	D1
13	$t'_{\rm FS}<t'_{\rm FR\text{-}CD}<t'_{\rm FR\text{-}RS}$	S
14	$t'_{\rm FS}<t'_{\rm FR\text{-}CD}<t'_{\rm RS}<t'_{\rm RR\text{-}FR}$	D1
15	$t'_{\rm FS}<t'_{\rm RS}<t'_{\rm FR\text{-}CD}<t'_{\rm RR\text{-}FR}$	D1
16	$t'_{\rm FS}<t'_{\rm RS}<t'_{\rm RR\text{-}CD}<t'_{\rm RR\text{-}FR}$	T
	$\rho_s=\rho_r$	
17	$t'_{\rm RS}<t'_{\rm RR\text{-}FS}$	S
18	$t'_{\rm RS}<t'_{\rm FS}<t'_{\rm RR\text{-}FR}$	D1
19	$t'_{\rm FS}<t'_{\rm FR\text{-}RS}$	S
20	$t'_{\rm FS}<t'_{\rm RS}<t'_{\rm RR\text{-}FR}$	D1

[a] Notations are given in § 2.2.
[b] Representative profiles of S, D1, D2, and T are schematically shown in Fig. 2.

3.1.2. *GRBs and Blazars*

Here we apply the above general consideration to the specific cases and examine which kind of rest-mass density profile is realized in GRBs and blazars. We assume that the widths of two shells are same in the ISM frame, which is written as $\Delta_r/\Delta_s=1$ (see, e.g., KS01). We consider the following three cases since it seems natural to suppose that ejected shells from the central engine have a correlation among them: (1) the energy of the bulk motion of the rapid shell ($E=\Gamma mc^2$) equals that of the slow one in the ISM frame (hereafter "equal energy" or "equal E"), (2) the mass of the rapid shell ($m=\rho\Gamma\Delta$) equals that of the slow one (hereafter "equal mass" or "equal m"), and (3) the rest-mass density of rapid shell equals that of the slow one (hereafter "equal rest-mass density" or "equal ρ"),

$$\begin{aligned}\rho_r&=\rho_s\ (\text{equal }\rho),\\ \rho_r\Delta_r\Gamma_r&=\rho_s\Delta_s\Gamma_s\ (\text{equal }m),\\ \rho_r\Delta_r\Gamma_r^2c^2&=\rho_s\Delta_s\Gamma_s^2c^2\ (\text{equal }E).\end{aligned}\tag{16}$$

Note that in the case of $\Delta_r=\Delta_s$ and $\Gamma_r>\Gamma_s$, ρ_s is always larger than ρ_r. This leads to the absence of $t_{\rm RR\text{-}FS}$. For all cases, we have $3+1+1=5$ parameters. We take the ratio

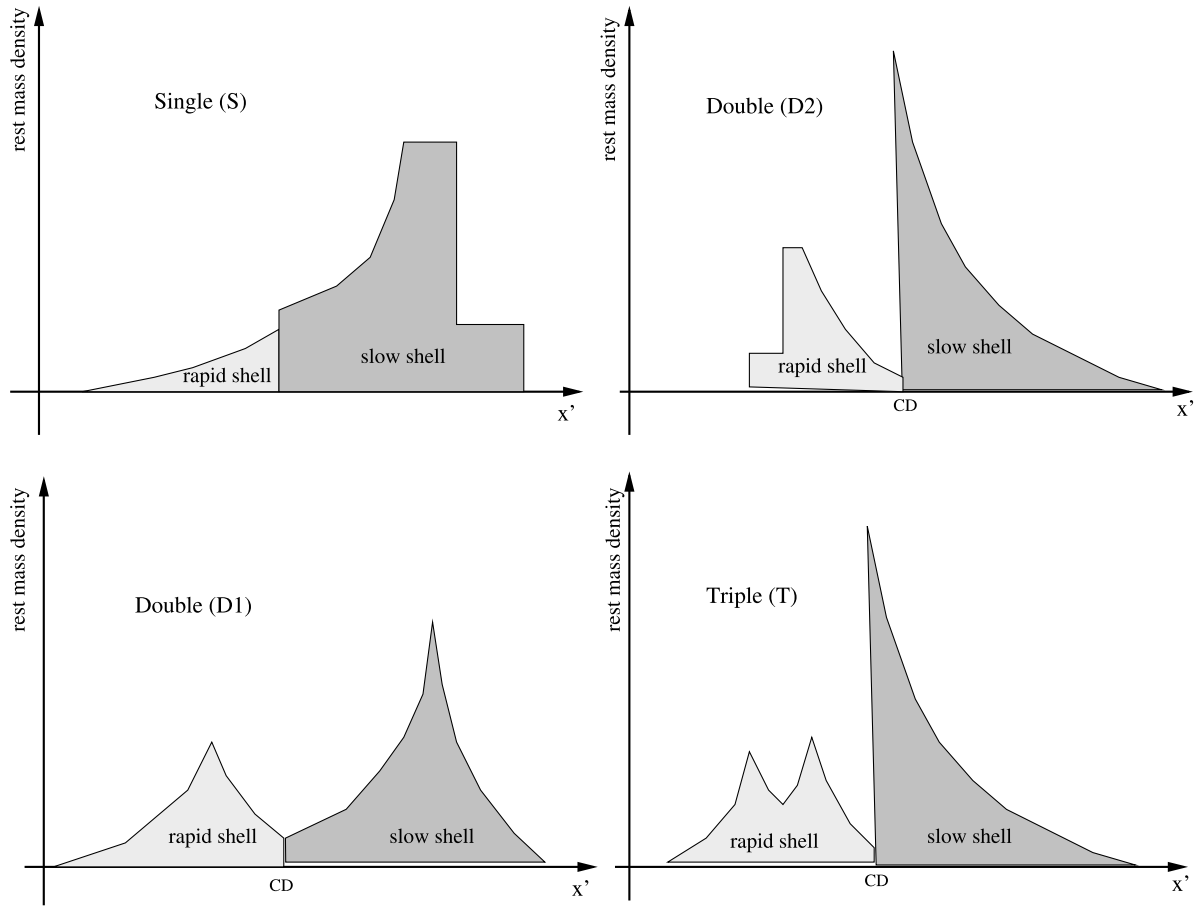

FIG. 2.—Schematic snapshot of the rest-mass density of two shells. Here we assume $\rho_s > \rho_r$. The corresponding timescale relation in each case is shown in Table 1. Picture S shows the case in which RR catches up with the propagating FS and has a single peak. Picture D1 shows the case in which both FS and RS cross the shells and the rarefaction wave propagating from both sides dig a dip and give a double-peaked profile. Picture D2 shows the case in which FR reaches CD and digs a dip. Hence, the profile is double-peaked. Picture T shows the case of the combination of D1 and D2. Then the final profile is triple-peaked.

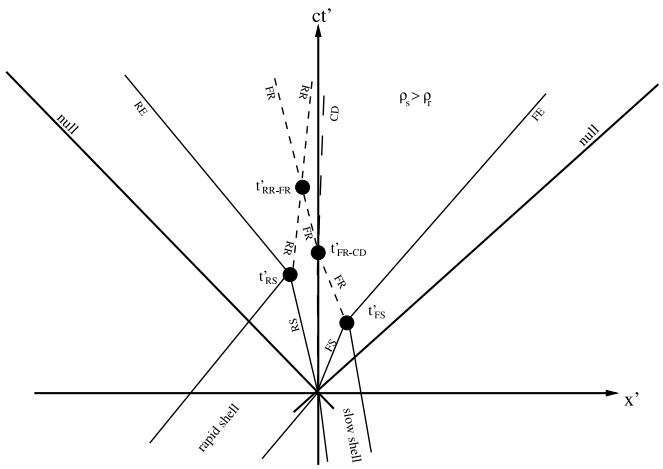

FIG. 3.—Schematic picture of spacetime diagram of a two-shell interaction in the CD frame. Here we assume $\rho_s > \rho_r$. A forward shock (FS) and a reverse shock (RS) run through the slow and rapid shells, respectively. After the shocks break out, the rarefaction waves propagate into the shells (FR and RR), and the shells spread (FE and RE). This corresponds to case 7 in Table 1.

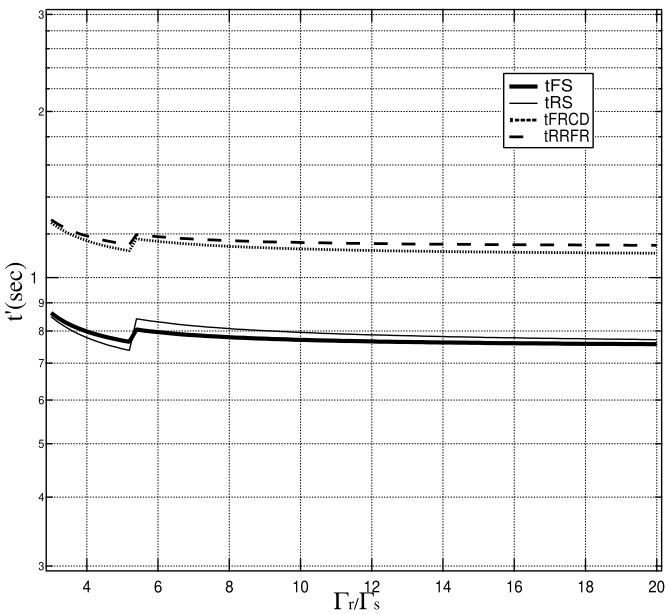

FIG. 4.—The Γ_r/Γ_s dependence of the various timescales for the equal-E case. In the whole range, case 4 (triple) is realized. The slight jumps of the timescales at $\Gamma_r/\Gamma_s \sim 5$ correspond to the abrupt change of adiabatic index. The softening of the EOS in the relativistic regime gives slower shock waves, and the timescales become longer accordingly.

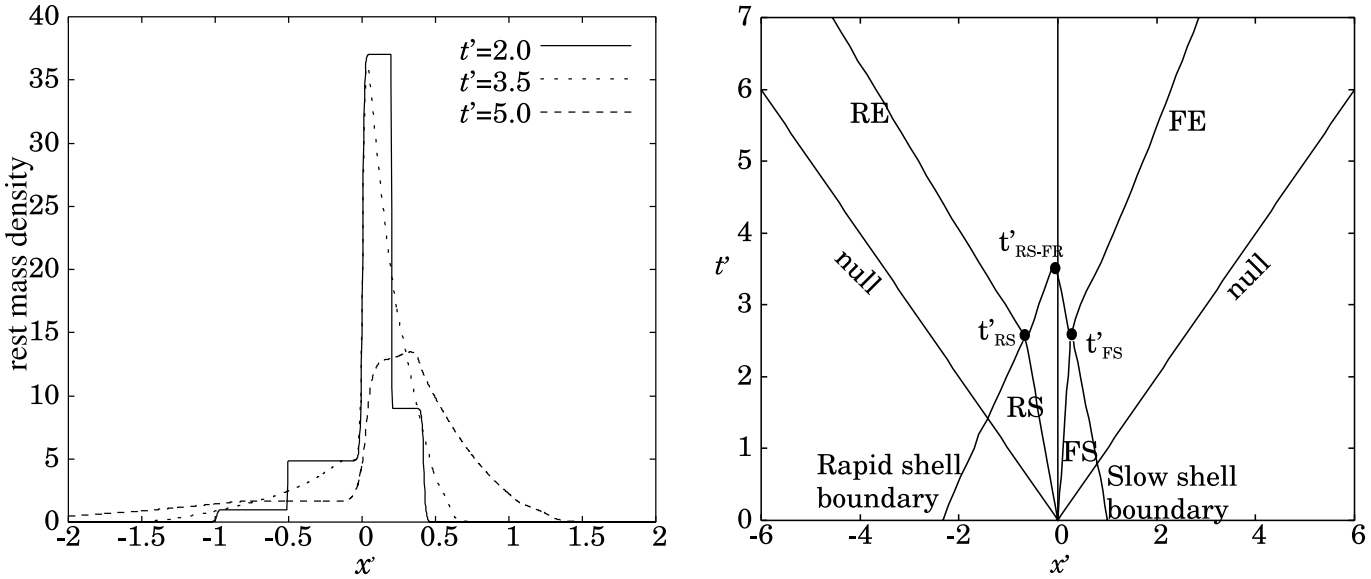

FIG. 5.—*Left*: Time evolution of the rest-mass density profile in the CD frame in the case of equal E. The parameter is chosen so that $\Gamma_r/\Gamma_s = 3$ in the ISM frame. The parameters in the CD frame are shown in Table 2. Throughout our numerical simulations, we set $\Delta_s'/c = 1$ and $\rho_s = 1$ as units. *Right*: Spacetime diagram of shock and rarefaction wave propagations. As shown in the text, $t_{\rm RS} \sim t_{\rm FS} \sim 3$. RE spreads at the speed $\sim 0.9c$, while FE spreads at the speed $\sim 0.6c$.

Γ_r/Γ_s as the last parameter and vary its value. This completes the six model parameters.

The various timescales for the equal-E case in GRBs are shown as a function of Γ_r/Γ_s in Figure 4. Here we set $\Gamma_s = 10^2$, $\Delta_s' = 10^{10}$ cm, and $\rho_s = 10^{-10}$ g cm^{-3} in the slow shell as an example. Slight jumps of timescales are seen at $\Gamma_r/\Gamma_s \sim 5$ in the figure. They are caused by the abrupt change of adiabatic index between the nonrelativistic and relativistic regimes. The softening of the EOS in the relativistic regime leads to slower shock wave propagation in the CD frame. In the whole range, criteria 1 and 2 given in § 3.1.1 are both satisfied. Therefore, the triple-peaked profile is expected (No. 4 in Table 1) in principle. However, criterion 1 is only marginally satisfied. As a result, the two peaks are not remarkable. It is worthwhile to obtain order estimations of Δ_r'/Δ_s' and $|\beta_r'/\beta_s'|$ by using a simple approximation of $\Gamma_{\rm CD} \sim \Gamma_m$ (Γ_m is the Lorentz factor of the merged shell obtained by the two-mass collision model, and it is given in § 3.3.1) in spite of some discrepancy with the exact solution of equation (5). We have

$$\frac{\Delta_r'}{\Delta_s'} = \frac{\Delta_r \Gamma_r \Gamma_s'}{\Delta_s \Gamma_s \Gamma_r'} \simeq \left(\frac{\Gamma_4}{\Gamma_1}\right)^2 \left(\frac{\Gamma_1^2 + \Gamma_2^2}{\Gamma_3^2 + \Gamma_4^2}\right),$$
$$\left|\frac{\beta_r'}{\beta_s'}\right| \simeq \frac{(\Gamma_1^2 + \Gamma_2^2)(-\Gamma_3^2 + \Gamma_4^2)}{(-\Gamma_1^2 + \Gamma_2^2)(\Gamma_3^2 + \Gamma_4^2)}. \quad (17)$$

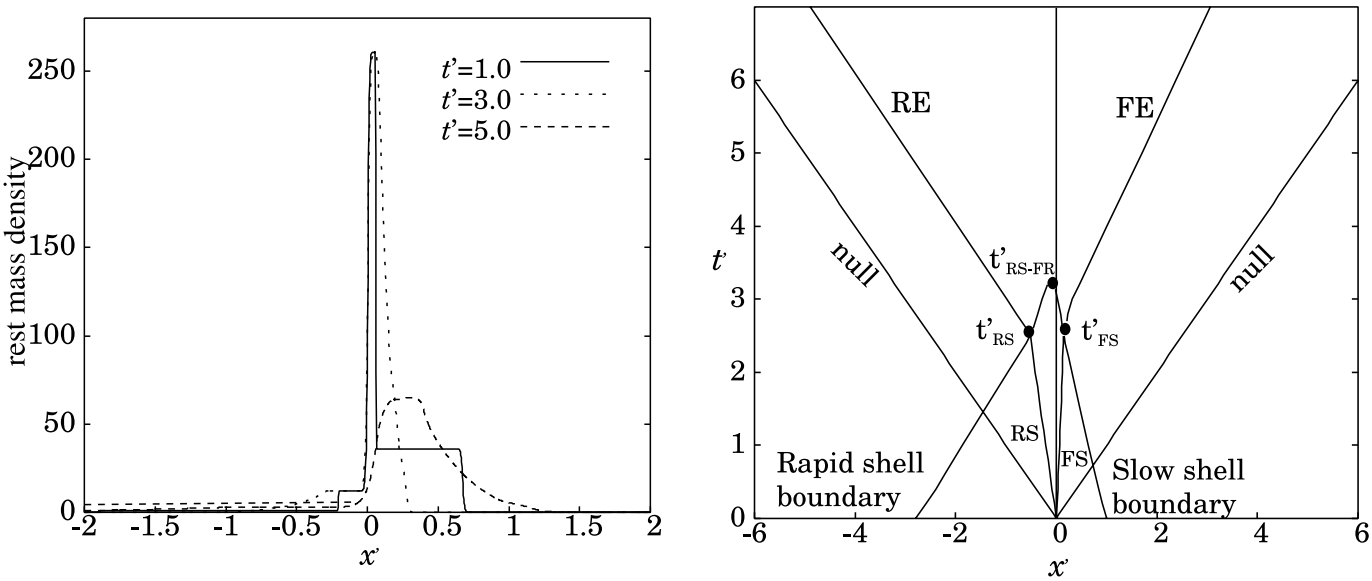

FIG. 6.—*Left*: Time evolution of the rest-mass density profile in the CD frame for equal E. In the ISM frame, $\Gamma_r/\Gamma_s = 6$. The parameters are given in Table 2. *Right*: Spacetime diagram of shock and rarefaction wave propagations. Both FS and RS propagate faster than those for $\Gamma_r/\Gamma_s = 3$ and $t_{\rm FS} \sim t_{\rm RS} \sim 3$. RE spreads at the speed $\sim c$, while FE spreads at the speed $\sim 0.7c$.

TABLE 2
PARAMETER SETS FOR NUMERICAL SIMULATIONS OF EQUAL E, EQUAL m, AND EQUAL ρ

Number[a]	Γ_r/Γ_s	Γ_{CD}[b]	Γ'_r	Γ'_s	Δ'_r/Δ'_s	ρ_s/ρ_r
4 (equal E).....	3	6.7	1.34	1.05	2.3	9
4 (equal E)[c]	6	7.0	2.26	1.06	2.8	36
6 (equal m).....	3	7.6	1.25	1.09	2.6	3
5 (equal m)[c]	20	11.8	4.29	1.40	6.4	20
19 (equal ρ).....	6	12.2	1.43	1.43	6.0	1
(equal ρ)[c,d]	20	22.4	2.35	2.35	1.0	1

[a] These numbers correspond to those shown in Table 1.
[b] The values are obtained by solving eq. (5). The slow shell Lorentz factor is fixed as $\Gamma_s = 5$.
[c] We use $\hat{\gamma}_3 = 4/3$.
[d] This corresponds to the case D1 profile in Fig. 2 without the assumption of $\Delta_s = \Delta_r$.

As Γ_r/Γ_s increases, the ratios of shell widths and velocities in the CD frame go asymptotically to

$$\frac{\Delta'_r}{\Delta'_s} \sim 3, \quad \left|\frac{\beta'_r}{\beta'_s}\right| \sim 3. \tag{18}$$

This equation explains well the fact that each timescale in Figure 4 has a weak dependence on Γ_r/Γ_s. This is why t'_{RS} and t'_{FS} are very close to each other; $t'_{RR\text{-}CD}$ is also close to $t'_{FR\text{-}CD}$ simply because the sound speeds in the both shocked regions are about a few 10% of the light speed and close to each other. The corresponding numerical results are shown in Figures 5 and 6. In these calculations, we take the cases of $\Gamma_r/\Gamma_s = 3$ and $\Gamma_r/\Gamma_s = 6$, respectively. This implies a large density contrast of $\rho_s/\rho_r = 9$ and $\rho_s/\rho_r = 36$, respectively (see Table 2). The collision of the rarefaction waves occurs in the region with much lower density compared with region 2. As a result, the peak of the profile is smoothed out. For larger values of Γ_r/Γ_s, the density contrast between regions 2 and 3 becomes clearer. Hence, we conclude that the equal-energy case essentially evolves into single-peaked profiles. The spacetime diagram obtained by the numerical simulation for equal E is shown in Figures 5 and 6. From Figure 5 we see that $t'_{FS} \sim t'_{RS} \sim 3$, as is shown in equation (18). In Figure 6, these timescales become close to 3.

The timescales for the equal-mass case are shown in Figure 7. Up to $\Gamma_r/\Gamma_s \sim 20$, criteria 1 and 2 are both satisfied and the triple-peaked profile shows up (No. 6 in Table 1). As Γ_r/Γ_s increases, we obtain

$$\frac{\Delta'_r}{\Delta'_s} \sim \frac{\Gamma_4}{\Gamma_1}, \quad \left|\frac{\beta'_r}{\beta'_s}\right| \sim 1, \tag{19}$$

and t'_{RS} and $t'_{RR\text{-}CD}$ become larger compared with t'_{FS} and $t'_{FR\text{-}CD}$. For the numerical experiment, we select two cases that have $\Gamma_r/\Gamma_s = 3$ and 20. In each case, we clearly see the dip corresponding to criterion 1 in Figures 8 and 9. However, as in the equal-E case, the collision of rarefaction waves occurs in the less dense rapid shell, and the density peak tends to be smoothed out. Hence, we conclude that the equal-mass collision with a large value of Γ_r/Γ_s effectively evolves into the double-peaked (D2) profile. In KS01, the authors found a shell-split feature in their numerical simulation (Fig. 2 in their paper) for the equal-m case. It can also be explained as the D2 profile. In Figure 9, we see that the rarefaction wave (FR) driven by the breakout of FS catches up with the shock wave (RS) from behind at $t' \sim 3$, since the flow seen from RS is subsonic in the downstream of RS. The propagation speed of RS is modified by the merge with the rarefaction wave and is determined by the strengths of the shock wave and rarefaction wave. For the current case, the propagation speed of RS is almost unchanged up to its breakout at $t' \lesssim 5.4$.

The timescales for the equal-ρ case is shown in Figure 10. The important point is that $\rho_s = \rho_r$ along CD. Then criterion 1 disappears. In the limit of large Γ_r/Γ_s, we have

$$\frac{\Delta'_r}{\Delta'_s} \sim \frac{1}{3}\left(\frac{\Gamma_4}{\Gamma_1}\right)^2, \quad \left|\frac{\beta'_r}{\beta'_s}\right| \sim \frac{1}{3}, \tag{20}$$

and t_{RS} and $t_{RR\text{-}CD}$ become larger compared with t_{FS} and $t_{FR\text{-}CD}$. We see this in the numerical experiment with $\Gamma_r/\Gamma_s = 6$ in Figure 11. As in Figure 9, we see also in Figure 11 that FR catches up to RS and merges during $3 \lesssim t' \lesssim 6.5$. The last topic is the dependence of the above results on the hitherto fixed model parameters Γ_s, Δ'_s, and ρ_s. The results for different Γ_s are

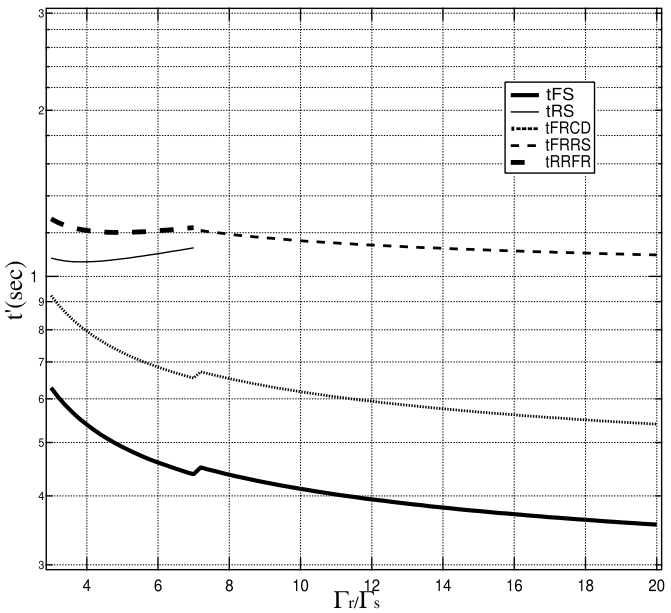

FIG. 7.—Timescales for equal mass. When Γ_r/Γ_s is smaller than $\sim$7, case 6 (triple) is realized. For Γ_r/Γ_s larger than $\sim$7, case 5 (D2) is realized. The slight jumps of the timescales at $\Gamma_r/\Gamma_s \sim 7$ correspond to the abrupt change of adiabatic index. The softening of the EOS in the relativistic regime gives slower shock waves, and the timescales become longer accordingly.

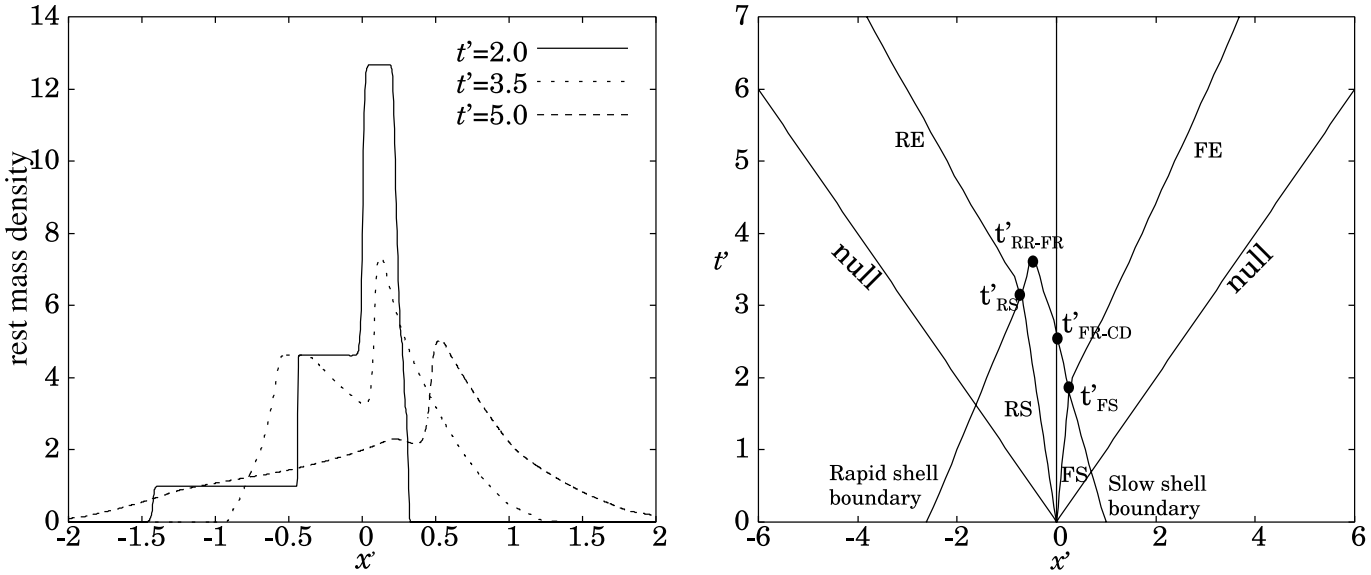

FIG. 8.—*Left*: Time evolution of the rest-mass density profile in the CD frame for equal m. In the ISM frame $\Gamma_r/\Gamma_s = 3$. The parameters are shown in Table 2. Criterion 2 is satisfied and the profile classified D2 in Fig. 2 is seen in this numerical result. *Right*: Spacetime diagram of shock and rarefaction wave propagations. RE spreads at the speed $\sim 0.8c$, while FE spreads at the speed $\sim 0.7c$.

completely the same as in Figure 4. The position of each timescale is determined by Δ_r'/Δ_s' and β_r'/β_s' and are independent of Δ_s itself. Hence, we omit corresponding figures. For different ρ_s the result is also almost unchanged, since we treat the case of $\Gamma_r/\Gamma_s > 3$ for simplicity. Then the sound speed is about a few 10% of the light speed and has a weak dependence on ρ_s. When Δ_s' is increased, every timescale increases linearly, keeping the relative positions of the timescales.

For a typical blazar, we set up three slow shell parameters as $\Gamma_s = 10$, $\Delta_s' = 10^{16}$ cm, and $\rho_s = 10^{-26}$ g cm^{-3}. We show the result in Figure 12 for the equal-E case as an example. The essential difference between GRBs and blazars is a typical shell width. Hence, as explained above, every timescale becomes 10^6 times larger than that in Figure 4 with the relative positions unchanged.

3.1.3. *Extra Case*

Since we have not seen a clear case corresponding to criterion 2 so far, we have performed another specific case to show what happens for the collision of two rarefaction-rarefaction waves (D1 profile in Fig. 2). The D1 profile appears most clearly when the rapid and slow shells have similar mass densities and shell widths in the CD frame. Hence, we do not use the assumption of $\Delta_r = \Delta_s$ here only. Instead, we employ the condition that $\rho_r = \rho_s$, $\Delta_r' = \Delta_s'$, and $\Gamma_r/\Gamma_s = 20$. In Figure 13, the D1 profile is indeed produced.

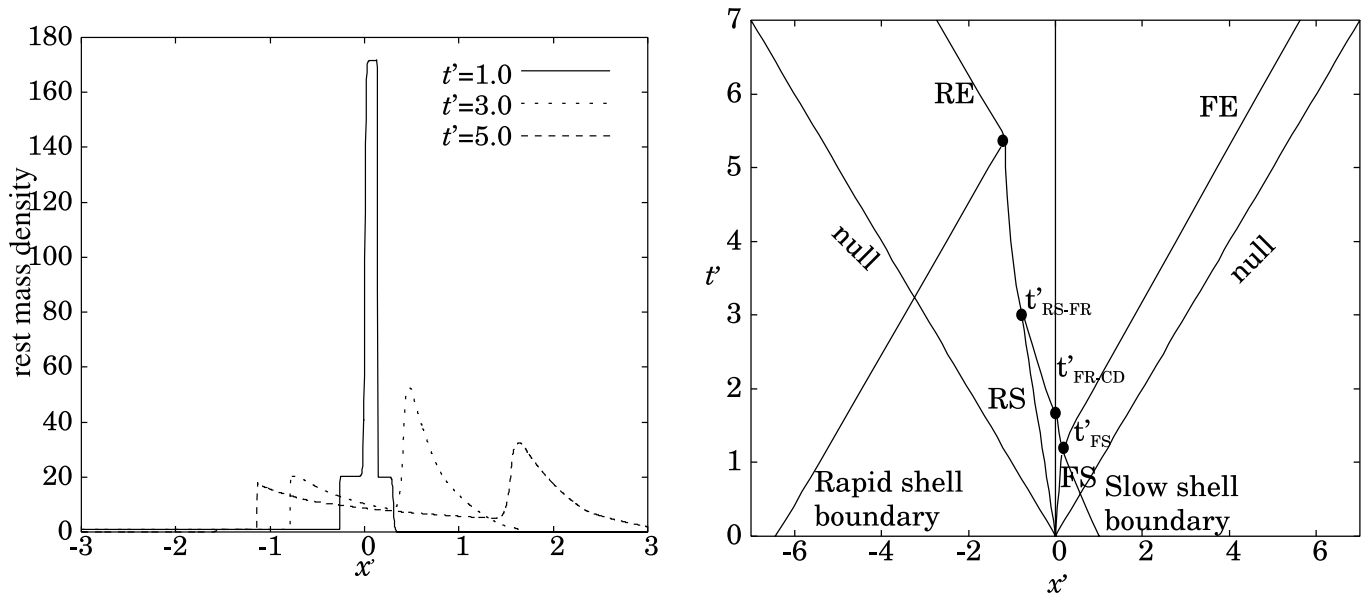

FIG. 9.—*Left*: Time evolution of the rest-mass density profile in the CD frame for equal m. In the ISM frame, $\Gamma_r/\Gamma_s = 20$. The parameters are shown in Table 2. The dilute rapid shell collides with the slow one and quickly spreads out. We also see that the dense slow shock is pushed forward by the rapid shell. *Right*: Spacetime diagram of shock and rarefaction wave propagations. RE spreads at the speed $\sim c$, while FE spreads at the speed $\sim 0.9c$.

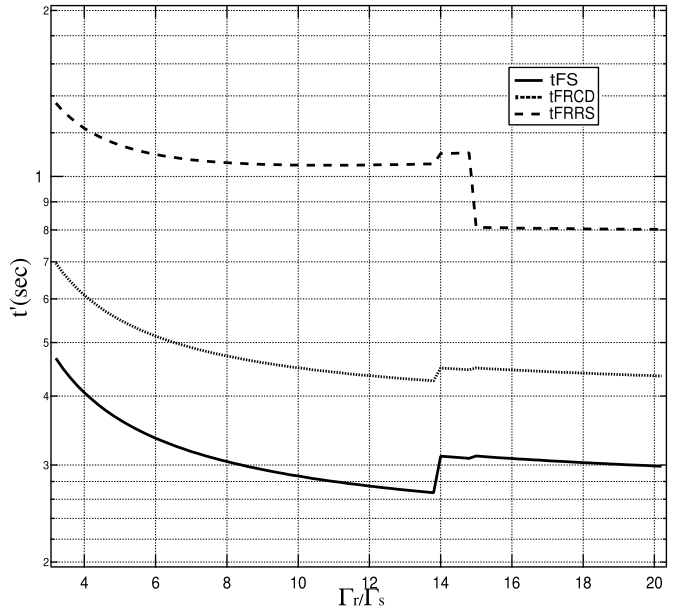

FIG. 10.—Timescales for equal ρ. Case 19 in Table 1 is realized in the whole range. The slight jumps of the timescales at $\Gamma_r/\Gamma_s \sim 14{,}15$ correspond to the abrupt change of adiabatic index. The softening of the EOS in the relativistic regime gives slower shock waves, and the timescales become longer accordingly.

A larger value of Γ_r/Γ_s produces a greater dip than that shown in Figure 13.

3.2. *Shell Spreading*

In principle, we can obtain the speed of the rarefaction wave using Riemann invariants (e.g., Zel'dovich & Raizer 1966). In the relativistic limit, it is known that the speed of the head of the rarefaction wave is close to the speed of light (e.g., Anile 1989). As the EOS of the shocked region deviates from the relativistic one, the speed is reduced from the light speed, and the intermediate regime should be treated by numerical calculations (e.g., Wen et al. 1997). It is worthwhile to note that from the values Γ_r' and Γ_s' in Table 2 we see that the EOS in the forward shocked region is a nonrelativistic one, while the reverse shocked region extends from the nonrelativistic to the relativistic regime for the parameter ranges we adopted.

Numerical results for shell spreading are shown in Figures 5, 6, 8, 9, and 11, in which the width of the shell may be described as

$$\Delta'_{\rm tot}(t') \simeq \Delta'_{s,\rm FS} + \Delta'_{r,\rm RS} + v_{\rm FE}(t' - t'_{\rm FS}) + v_{\rm RE}(t' - t'_{\rm RS}), \quad (21)$$

where $\Delta'_{\rm tot}$ is the total width of the shell in the CD frame. We should stress that although many authors assume that the shell width is not changed after collisions (e.g., Spada et al. 2001; NP02) for simplicity, the reality is that the shells spread at $v_{\rm FE}$ and $v_{\rm RE}$ in the forward and backward directions, respectively.

3.3. *Energy Conversion Efficiency*

The conversion efficiency of the bulk kinetic energy to the internal one is one of the most important issues in exploring the nature of the central engine of relativistic outflows, and many authors have studied it (e.g., Kumar 1999; Tanihata et al. 2003).

3.3.1. *Two-Mass Collision Model*

Let us briefly review the widely used two-mass collision model (e.g., Piran 1999). From the momentum and energy conservations, we have

$$\begin{aligned} m_r\Gamma_r + m_s\Gamma_s &= (m_m + \mathcal{E}_m/c^2)\Gamma_m, \\ m_r\Gamma_r\beta_r + m_s\Gamma_s\beta_s &= (m_m + \mathcal{E}_m/c^2)\Gamma_m\beta_m, \end{aligned} \quad (22)$$

where $m_m = m_r + m_s$, $\mathcal{E}_m = \mathcal{E}_r + \mathcal{E}_s$, and Γ_m are the mass, the internal energy, and the Lorentz factor of the merged shell, respectively, and m_r and m_s are the rest mass of the rapid and slow shells, respectively. Then we obtain the efficiency ϵ as

$$\epsilon = 1 - \frac{(m_r + m_s)\Gamma_m}{m_r\Gamma_r + m_s\Gamma_s}, \quad \Gamma_m^2 = \Gamma_r\Gamma_s\frac{m_r\Gamma_r + m_s\Gamma_s}{m_r\Gamma_s + m_s\Gamma_r}. \quad (23)$$

It is a useful shortcut to approximate $\Gamma_m \sim \Gamma_2 = \Gamma_3$ without solving equation (5). Using this shortcut for the equal-mass density case ($m_r/\Gamma_r = m_s/\Gamma_s$), we have $\Gamma_m^2 = (\Gamma_r^2 + \Gamma_s^2)/2$.

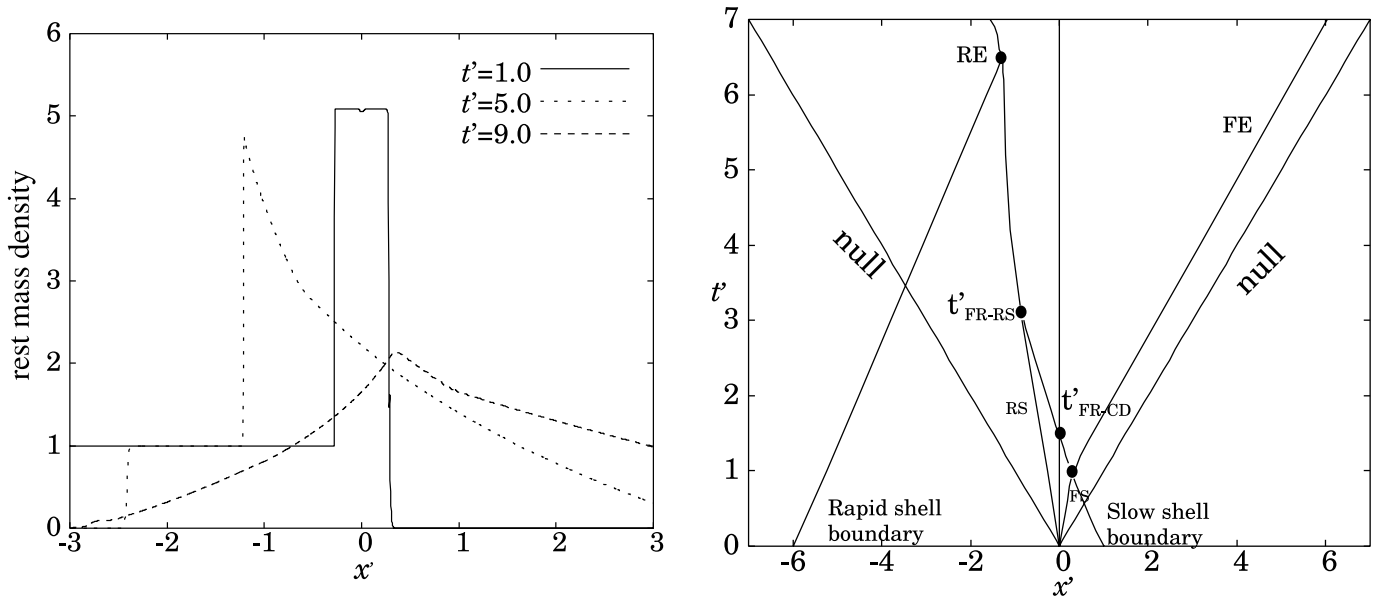

FIG. 11.—*Left*: Time evolution of the rest-mass density profile in the CD frame for equal ρ. In the ISM frame, $\Gamma_r/\Gamma_s = 6$. The parameters are shown in Table 2. *Right*: Spacetime diagram of shock and rarefaction wave propagations. RE spreads at the speed $\sim c$, while FE spreads at the speed $\sim 0.8c$.

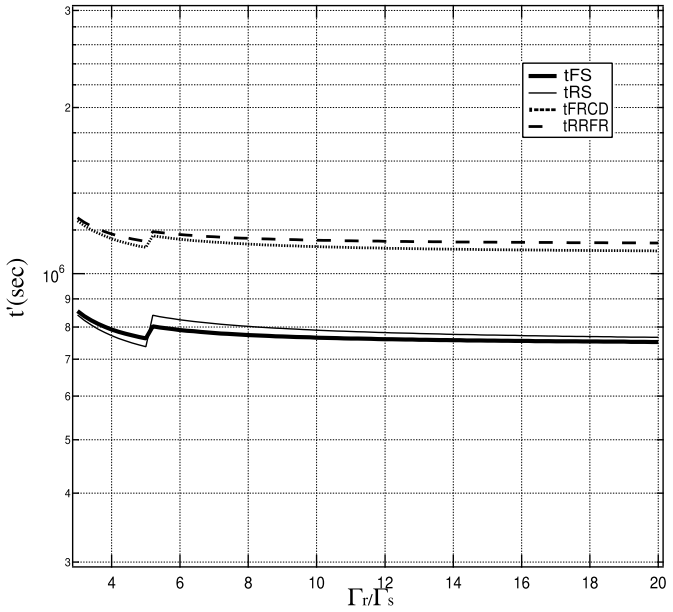

FIG. 12.—Same as Fig. 4, but for blazars. Compared with Fig. 4 the relative positions of various timescales are almost unchanged, while the absolute value of each timescale is reduced by a factor of 10^6, which is the ratio of the shell width of GRB to that of the blazar.

For the equal-mass case ($m_r = m_s$), we have $\Gamma_m^2 = \Gamma_r\Gamma_s$. For equal energy ($m_r\Gamma_r = m_s\Gamma_s$), we have $\Gamma_m^2 = 2(\Gamma_s^2\Gamma_r^2)/(\Gamma_s^2 + \Gamma_r^2)$. Then, the efficiency ϵ in each case is given by

$$\epsilon \simeq \begin{cases} 1 - \dfrac{1}{\sqrt{2}}\left(1 + \dfrac{\Gamma_s}{\Gamma_r}\right)\left[1 + \left(\dfrac{\Gamma_s}{\Gamma_r}\right)^2\right]^{-1/2} & \text{(equal } \rho\text{)}, \\ 1 - \left[\dfrac{4}{2 + (\Gamma_r/\Gamma_s) + (\Gamma_s/\Gamma_r)}\right]^{1/2} & \text{(equal } m\text{)}, \\ 1 - \dfrac{1}{\sqrt{2}}\left(1 + \dfrac{\Gamma_r}{\Gamma_s}\right)\left[1 + \left(\dfrac{\Gamma_r}{\Gamma_s}\right)^2\right]^{-1/2} & \text{(equal } E\text{)}. \end{cases} \quad (24)$$

As the value of Γ_r/Γ_s gets larger for the equal-m case, the efficiency becomes larger and approaches $\sim$1. For the equal-E and equal-ρ cases, it goes asymptotically to $\sim$0.3. Thus, we find that equal m is the most effective collision if we neglect the rarefaction waves.

3.3.2. *Shock Model*

The consideration of shock dynamics provides us with information on the assignment of the total dissipation energy $E_{\rm diss}$ to the forward and reverse shocked regions, $E_{\rm FS}$ and $E_{\rm RS}$. From the equations of mass continuity in the CD frame, we have $\Delta'_{s,\rm FS}/\Delta'_s = [\Gamma'_1(\hat{\gamma}_2 - 1)]/(\hat{\gamma}_2\Gamma'_1 + 1)$ and $\Delta'_{s,\rm RS}/\Delta'_r = [\Gamma'_4(\hat{\gamma}_3 - 1)]/(\hat{\gamma}_3\Gamma'_4 + 1)$. Assuming a large value of Γ_4/Γ_1, we have $e_2 + P_2 \simeq e_3 + P_3$, and the dissipated energies are mainly controlled by shell widths. They are written as

$$\frac{E_{\rm FS}}{E_{\rm diss}} \simeq \frac{\Delta'_{s,\rm FS}}{\Delta'_{s,\rm FS} + \Delta'_{r,\rm RS}}, \quad \frac{E_{\rm RS}}{E_{\rm diss}} \simeq \frac{\Delta'_{r,\rm RS}}{\Delta'_{s,\rm FS} + \Delta'_{r,\rm RS}}, \quad (25)$$

where $E_{\rm FS}$ and $E_{\rm RS}$ are the internal energy of forward and reverse shocked regions just after the shock crosses each shell, respectively (e.g., Spada et al. 2001). However, the values $E_{\rm FS}/E_{\rm diss}$ and $E_{\rm RS}/E_{\rm diss}$ will begin to deviate from the above approximation when the rarefaction waves start to propagate, since they reconvert internal energy into kinetic energy. The result including the rarefaction waves is shown below.

3.3.3. *Numerical Results*

The estimation of the energy conversion efficiencies with shock and rarefaction waves taken into account are presented in Figures 14, 15, and 16 based on the numerical simulations. From the analogy of the two-mass collision model, we define the efficiency measured in the ISM frame as

$$\epsilon(t) \equiv 1 - \frac{\int \Gamma(t,\ x)\, dm(t,\ x)}{\Gamma_r m_r + \Gamma_s m_s} = 1 - \frac{\int \Gamma(t,\ x)\rho(t,\ x)\Gamma(t,\ x)\, dx}{\rho_r\Delta_r\Gamma_r^2 + \rho_s\Delta_s\Gamma_s^2}, \quad (26)$$

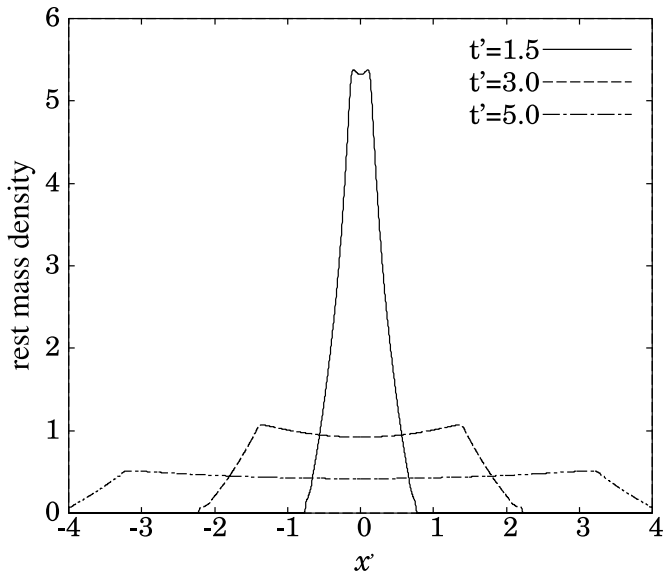

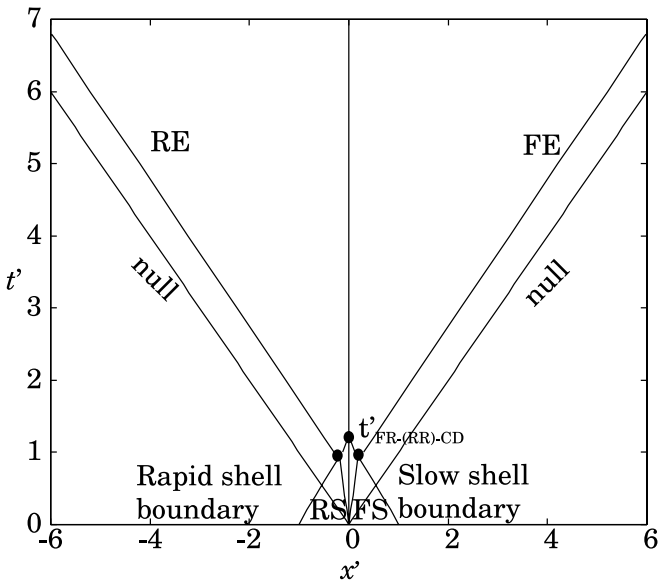

FIG. 13.—*Left*: Time evolution of the rest-mass density profile in the CD frame for equal ρ. In the ISM frame, $\Gamma_r/\Gamma_s = 20$. The parameters are shown in Table 2. By the rarefaction-rarefaction wave collision, the bump is generated at the center of the shell. This corresponds to the D1 profile in Fig. 2. *Right*: Spacetime diagram of shock and rarefaction wave propagations. Both RE and FE spread at the speed $\sim c$.

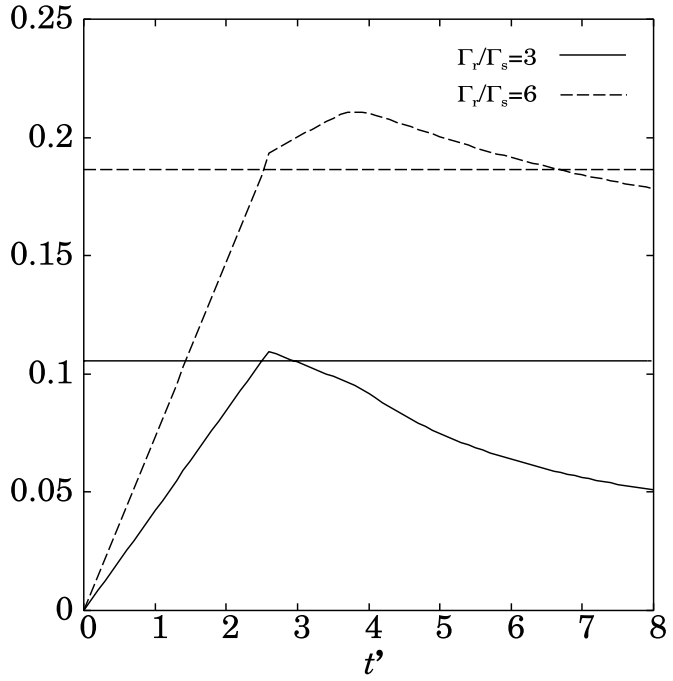

FIG. 14.—Time evolutions of the conversion efficiency defined by eq. (26) for the equal-energy case. During shock propagations, ϵ approaches the two-mass collision estimate given by eq. (24) for each case. As the rarefaction waves begin to propagate, the efficiencies are reduced by them. This suppression can be ascribed to the thermal expansion.

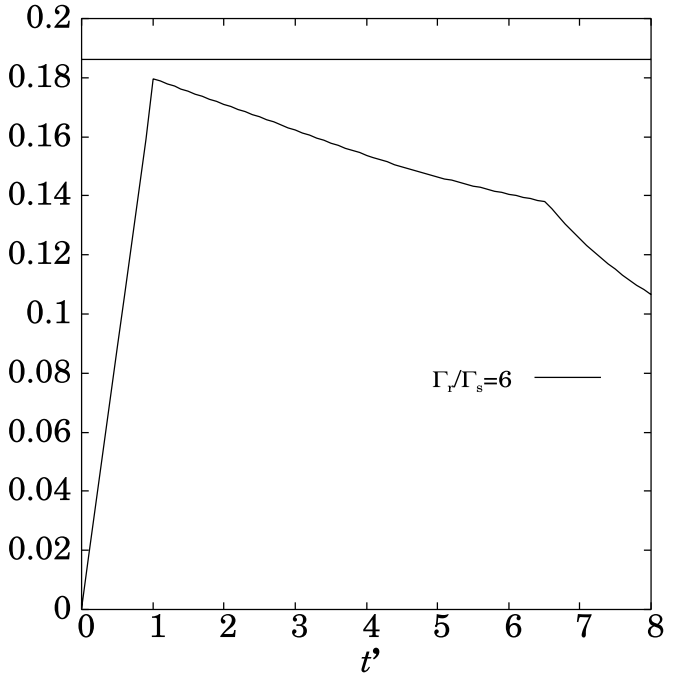

FIG. 16.—Time evolutions of the conversion efficiency defined by eq. (26) for the equal-ρ case. During shock propagations, ϵ approaches the two-point mass estimate given by eq. (24) for each case.

where $dm(t,x)$, $\rho(t,x)$, $\Gamma(t,x)$, and $\Gamma(t,x)\,dx$ are the rest-mass element, the rest-mass density, and the Lorentz factor, seen in the ISM frame, and the length of line element in the CD frame, respectively. We assume that the origins of both frames coincide at $t = t' = 0$. The Lorentz transformation of $\Gamma(t,x)$ is written as $\Gamma(t,x) = \Gamma_{\rm CD}\Gamma'(t,x)[1 - \beta_{\rm CD}\beta'(t,x)]$. The hypersurface of a constant time in the ISM frame does not coincide with that in the CD frame. Hence, to evaluate spatial integrations at a certain time in the ISM frame, we must collect the values of physical quantities in the integrand for different times in the CD frame. Unfortunately, this is a technically difficult task to perform. Hence, we report to an approximation that $\rho(t,x)$ and $\Gamma(t,x)$ are replaced by $\rho(t',x')$ and $\Gamma(t',x')$, respectively. This is only valid near the original point of the CD frame and mixes up these quantities at other time slices. We believe, however, that this still gives the behavior of the efficiency and the essential role of rarefaction waves. In these figures, we compare the numerical results with the prediction by the two-mass collision approximation. We find that the two-mass collision model well reproduces the hydrodynamic results just before the rarefaction waves begin to propagate. After the shock waves breakout of the shells, the conversion efficiency is reduced by several 10% from the estimate of the two-mass collision model after several dynamical times. It is noted again that no cooling effect is taken into account here.

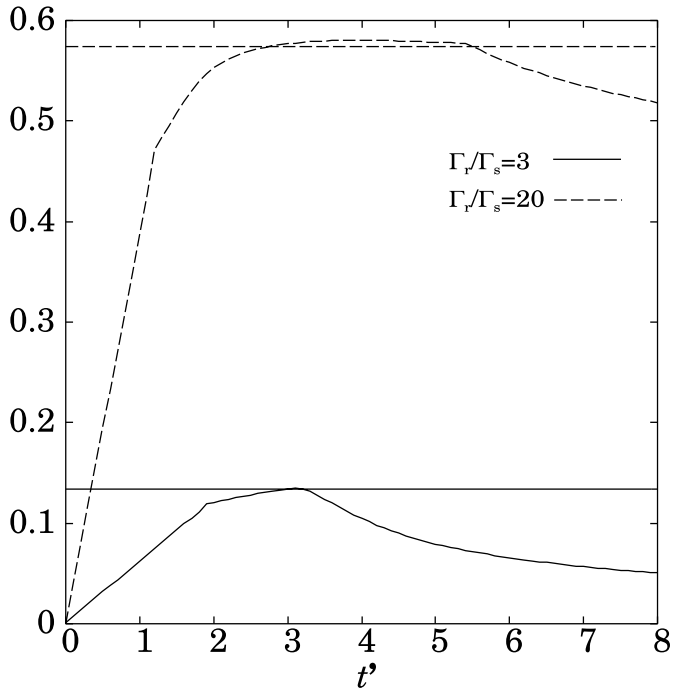

FIG. 15.—Time evolutions of the conversion efficiency defined by eq. (26) for the equal-m case. During shock propagations, ϵ approaches the two-point mass estimate given by eq. (24) for each case.

4. SUMMARY AND DISCUSSION

In this paper we have illuminated the difference between the simple two-mass collision model and the hydrodynamic model of the internal shock. We have studied one-dimensional hydrodynamic simulations of the two-shell collisions in the CD frame taking the shock and rarefaction waves into account. Below we summarize our results and give some discussions.

1. By comparing the relevant timescales of shock and rarefaction waves, we have completely classified the evolutions of the two-shell collisions using six physical parameters, that is, the widths, rest-mass densities, and velocities of the two colliding shells. We find that rarefaction waves have a significant effect on the dynamics. In principle, the rest-mass density profile can be evolved into single-, double-, and triple-peaked

features. In the limit of $\Gamma_r, \Gamma_s \gg 1$, the features are essentially characterized by only three parameters: the ratios of Lorentz factors, widths, and rest-mass densities. The combination of the values of Γ_r/Γ_s and ρ_r/ρ_s determines the relative orders of the timescales of various wave propagations, while the value of Δ_r/Δ_s controls the normalizations of the timescales.

2. Bearing in mind the application to relativistic outflows such as GRBs and blazars, we specifically examine the cases of equal ρ, equal m, and equal E. For the equal-ρ case, the profile is single-peaked. The rarefaction wave produced when FS breaks out reaches CD and then catches up with RS. In the case of equal m, the profile should in principle become triple-peaked according to our classification scheme. In practice, however, there is very little time for the FR-RR collision to make a clear dip, while there is a lot more time for FR to create a dip for a fairly wide range of parameters. Therefore, the profile in this case is effectively double-peaked. For the equal-E case, the profile is classified as triple-peaked. Again, however, there is very little time for the FR-RR collision to make a dip. A very large mass-density gradient between forward and reverse shocked regions makes the dip even less pronounced. Furthermore, there is again little time for FR to create a dip for a fairly wide range of parameters. Hence, we conclude that the profile for equal E is effectively single-peaked. If the cooling timescale is sufficiently long in the shocked region, electromagnetic radiation will show these profiles.

3. For large Γ_r/Γ_s, we have shown that the spreading velocity of the shells after collision is close to the speed of light. Hence, the often used approximation of constant shell width after collision is not very good in treating multiple collisions. For example, NP02 claim that the equal-energy case is suggested for the shell Lorentz factors in GRBs, assuming that $L > \Delta$, where L is the separation distance between two shells. If the interval of the first and the second collisions is long, however, the shell spreading effect cannot be ignored, and the case of $L < \Delta$ should be included in the analysis. Then the difference between the equal-m and equal-E cases might be wiped away.

4. As the shell spreads after collision, the internal energy is converted back to the bulk kinetic energy because of thermal expansion. We have numerically studied the time-dependent energy conversion efficiency quantitatively. Since we have neglected the cooling processes, the conversion efficiency rises up to the order of unity. This should correspond to the event in the regime of "weak cooling" (Kino & Takahara 2004). If $\Gamma_r/\Gamma_s \gg 1$ and the time interval between collisions is long, the conversion efficiency will be substantially deviated the estimate of the two-mass collision model.

We appreciate the insightful comments and suggestions of the referee. M. K. thanks S. Kobayashi, K. Asano, and F. Takahara for useful remarks and discussions. A. M. acknowledges support from the Japan Society for the Promotion of Science (JSPS). This work is also supported in part by the Grant-in-Aid Program for Scientific Research (14340066, 14740166, and 14079202) from the Ministry of Education, Science, Sports, and Culture of Japan.

REFERENCES

Anile, A. M. 1989, Relativistic Fluids and Magnetofluids (Cambridge: Cambridge Univ. Press)
Blandford, R. D., & McKee, C. F. 1976, Phys. Fluids, 19, 1130
Donat, R., & Marquina, A. 1996, J. Comput. Phys., 125, 42
Fishman, G. J., & Meegan, C. A. 1995, ARA&A, 33, 415
Kino, M., & Takahara, F. 2004, MNRAS, 349, 336
Kino, M., Takahara, F., & Kusunose, M. 2002, ApJ, 564, 97
Kobayashi, S., Piran, T., & Sari, R. 1997, ApJ, 490, 92 (KPS97)
Kobayashi, S., & Sari, R. 2001, ApJ, 551, 934 (KS01)
Kumar, P. 1999, ApJ, 523, L113
Landau, L. D., & Lifshitz, E. M. 1959, Fluid Mechanics (Oxford: Pergamon Press)
Mihalas, D., & Mihalas, B.W. 1984, Foundations of Radiation Hydrodynamics (Oxford: Oxford Univ. Press)
Mizuta, A., Yamada, S., & Takabe, H. 2004, ApJ, 606, 804
Nakar, E., & Piran, T. 2002, ApJ, 572, L139 (NP02)
Panaitescu, A., Wen, L., Laguna, P., & Meszaros, P. 1997, ApJ, 482, 942
Piran, T. 1999, Phys. Rep., 314, 575
Rees, M. J. 1978, MNRAS, 184, 61P
Rees, M. J., & Meszaros, P. 1994, ApJ, 430, L93
Sari, R., & Piran, T. 1995, ApJ, 455, L143
Spada, M., Ghisellini, G., Lazzati, D., & Celotti, A. 2001, MNRAS, 325, 1559
Takahashi, T., et al. 2000, ApJ, 542, L105
Tanihata, C., Takahashi, T., Kataoka, J., & Madejski, G. 2003, ApJ, 584, 153
Wen, L., Panaitescu, A., & Laguna, P. 1997, ApJ, 486, 919
Zel'dovich, Ya. B., & Raizer, Yu. P. 1966, Physics of Shock Waves and High-Temperature Phenomena (New York: Academic)